



# A recombination analysis of Cu(In,Ga)Se<sub>2</sub> solar cells with low and high Ga compositions

Jian V. Li<sup>\*</sup>, Sachit Grover, Miguel A. Contreras, Kannan Ramanathan, Darius Kuciauskas, Rommel Noufi

National Renewable Energy Laboratory, Golden, CO 80401, United States

## ARTICLE INFO

### Article history:

Received 1 September 2013

Received in revised form

22 November 2013

Accepted 19 January 2014

Available online 20 February 2014

### Keywords:

Recombination

CIGS

Interface

Open-circuit voltage

Bandgap

## ABSTRACT

Separation and quantification of recombination losses in thin-film Cu(In<sub>1-x</sub>Ga<sub>x</sub>)Se<sub>2</sub> solar cells is paramount to understanding the current state-of-the-art and future improvements, but an effective characterization technique has been lacking. We use the recently developed temperature–illumination-dependent open-circuit voltage method to extract individual recombination rates at the buffer/absorber interface, in the space-charge region, and in the quasi-neutral region, as well as the carrier lifetime and surface recombination velocity for devices with low ( $x=30\%$ ) and high ( $x=84\%$ ) Ga absorbers. In the low-Ga absorber, recombination in the quasi-neutral region dominates. In the high-Ga absorber, interface recombination dominates. The open-circuit voltage deficit of the high-Ga device originates from an inadequacy of band bending in the absorber and a lack of strong inversion at the buffer/absorber interface. As two promising mitigating strategies for the open-circuit voltage deficit problem at high-Ga levels, we highlight a homojunction in the absorber or alternative transparent conducting oxides with low work function.

© 2014 Elsevier B.V. All rights reserved.

## 1. Introduction

Cu(In<sub>1-x</sub>Ga<sub>x</sub>)Se<sub>2</sub> (CIGS) thin-film solar cells have achieved impressive power conversion efficiency and are promising for large-scale commercial deployment [1–3]. Further improvement of CIGS conversion technology critically depends on reducing the voltage deficit (i.e., the difference between the open-circuit voltage  $V_{OC}$  and bandgap energy of the absorber [4,6,7]) caused by recombination losses distributed across the device. The need to reduce recombination calls for a variety of tactics in material and device engineering, e.g., reducing defects in the absorber to improve minority-carrier lifetime [8], optimizing the buffer/absorber band offset to reduce surface recombination velocity at the interface [9,10], and engineering the heterojunction to maximize the built-in potential [9,10]. To assess the current CIGS state of the art and select appropriate engineering tactics, each recombination loss needs to be separated and quantified—an obvious goal that thus far has remained elusive.

The main tool for recombination analysis in the photovoltaic devices is the temperature-dependent open-circuit voltage  $V_{OC}(T)$  technique [11,12], which identifies the dominant recombination mechanism by the activation energy of the recombination extracted

from the intercept of  $V_{OC}(T)$  at  $T=0$  K. The technique has been used to qualitatively attribute the voltage deficit in high-bandgap CIGS devices to interface recombination [4,13–15]. However, no quantitative assessment of the recombination rates is possible because the existing technique uses only the 1-dimensional temperature dependence of  $V_{OC}$  at a fixed light intensity. We expanded the methodology [16] into an additional dimension by including the light-intensity (i.e., generation  $G$ ) dependence of  $V_{OC}$ . From the 2-dimensional dependence of  $V_{OC}(T, G)$ , the new method is capable of separating and quantifying recombination rates at the buffer/absorber interface, in the space-charge region (SCR), and in the quasi-neutral region (QNR), all at the  $V_{OC}$  point. Furthermore, it is possible to extract intrinsic material properties such as the minority-carrier lifetime in the absorber and surface recombination velocity at the interface.

We use the new method to study the recombination pathways in CIGS devices with low-Ga ( $x=30\%$ ) and high-Ga ( $x=84\%$ ) absorbers. New insights not previously available are provided by quantitative extractions of individual recombination rates at the buffer/absorber interface, in the SCR, and in the QNR, as well as the bulk minority-carrier lifetime and surface recombination velocity at the interface. In the high-bandgap absorbers, we discuss why interface recombination dominates the  $V_{OC}$  deficit. We find that inadequate band-bending and interface inversion are the main culprits for high interface recombination and discuss the relative effectiveness of mitigation strategies in the absorber, buffer, buffer/absorber interface, and transparent conducting oxide (TCO).

<sup>\*</sup> Corresponding author.

E-mail address: [jian.li@nrel.gov](mailto:jian.li@nrel.gov) (J.V. Li).

## 2. Experiment

The CIGS/buffer thin-film solar cells used in this study have the same structure as those described in Ref. [4]. Starting from the soda-lime glass substrate, a typical device consists of a 1- $\mu\text{m}$  Mo bilayer deposited by sputtering, 2- $\mu\text{m}$  CIGS absorber deposited by three-stage co-evaporation, 50-nm CdS buffer layer deposited by chemical-bath deposition, bilayer transparent conducting oxide of intrinsic (90 nm) and Al-doped (120 nm) ZnO deposited by sputtering, and a Ni/Al metal-grid front-contact. The devices studied in this work consist of CIGS absorbers with 30% and 84% Ga compositions, corresponding to bandgaps of 1.18 and 1.5 eV, respectively [5]. The 30% Ga composition was chosen because the highest-efficiency CIGS cell is of this composition. The 84% Ga composition was chosen because the voltage deficit is known to be very severe at this Ga composition. High-performance samples are used in this study to represent the current state of the art in the respective ranges of Ga composition [4].

The performance of the devices was measured under a standard AM1.5 condition. We used an Agilent B2912A source-measurement unit for the current-voltage measurement with varying temperature (70–310 K) and light intensity ( $1 \times 10^{-6}$  to 1 sun), the latter controlled by a set of neutral-density filters with a Newport 96000 solar simulator. We used an Agilent 4294 A impedance analyzer to conduct the capacitance-voltage (10 kHz, bias from  $-1.0$  to  $+0.5$  V) measurements. Time-resolved photoluminescence (TRPL) [17] was used to measure the minority-carrier lifetime. This measurement was performed on the absorber films, rather than completed devices, to avoid complication due to carrier extraction at the junction. Excitation wavelength was 780 nm, laser repetition rate was 1 MHz, and excitation spot size was 0.25 mm. Photoluminescence signals were measured with an appropriate long-pass filter.

## 3. Method

The formulation of  $V_{OC}$  dependence on generation  $G$ , temperature  $T$ , and recombination rate is detailed elsewhere [16]; below is a brief summary. Let  $R^i$ ,  $R^d$ , and  $R^b$  be the Shockley-Read-Hall [11,18] recombination rates, respectively, at the interface, in the SCR, and in the QNR under a bias  $V$ . In this work, the bias can be applied either by an electrical voltage or light at open circuit. Fig. 1 shows the relevant parameters in a band diagram. We express each recombination rate as the product of a  $V$ -independent recombination coefficient and an exponential function of  $V$

$$\begin{cases} R^i = R_0^i e^{qV/kT} \\ R^d = R_0^d e^{qV/2kT} \\ R^b = R_0^b e^{qV/kT} \end{cases} \quad (1)$$

$k$  is the Boltzmann constant.  $R_0^i$ ,  $R_0^d$ , and  $R_0^b$  are the  $V$ -independent recombination coefficients at the interface, in the SCR, and in the QNR, in that order. They are essentially the recombination rates at  $V=0$  V and account for the intrinsic material or device properties determining the effectiveness of the respective recombination pathways. The exponential functions of  $V$  account for the densities of the carriers limiting the respective recombination rates. Eq. (1) indicates that the ideality factor associated with  $R^i$  is 1, which is true when the Fermi energy is pinned and band bending is negligible in the buffer and TCO. Eq. (1) also indicates that the ideality factor associated with  $R^d$  is 2. This is true for recombination centers near midgap but may not be true if they are close to the bands [11,19], especially if tunneling is present [11], which can be the case for high-Ga compositions. In the latter case, the same approach described in this work is applicable, but the algebra

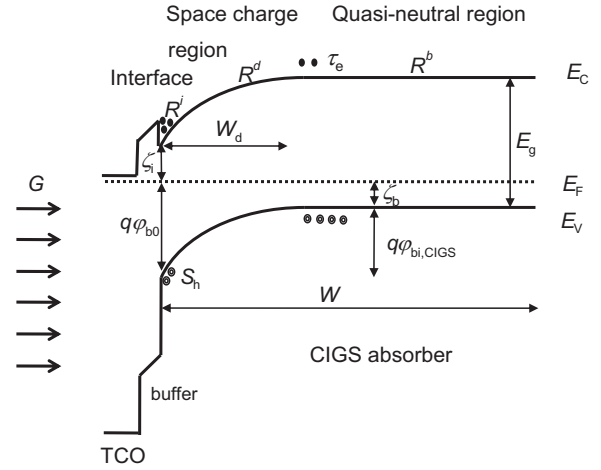


**Fig. 1.** Band diagram of a CIGS absorber at 0 V bias showing recombination rates in various locations and relevant parameters.  $G$  is the optical generation.  $R^i$ ,  $R^d$ , and  $R^b$  are the Shockley-Read-Hall recombination rates, respectively, at the interface, in the SCR, and in the QNR under a bias  $V$ .  $\zeta_i$  is the separation of Fermi energy  $E_F$  from the conduction band  $E_C$  at the buffer/absorber interface.  $\zeta_b$  the separation of Fermi energy  $E_F$  from the valence band  $E_V$  in the QNR of the absorber.  $\phi_{bi,CIGS}$  is the built-in voltage in the absorber.  $\phi_{b0}$  is the hole potential barrier at the buffer/absorber interface at zero bias. Note  $\phi_{b0} = \zeta_b + \phi_{bi,CIGS}$ .  $S_h$  is the surface recombination velocity for holes at the buffer/absorber interface.  $W_d$  is the depletion width in the absorber.  $\tau_e$  is the electron lifetime in the absorber.

needs to be modified. Eq. (1) and all derivations in Ref. [16] are valid even if the quasi-Fermi level separation is not constantly  $V$  in the entire QNR, as long as the total integrated recombination rate in the QNR  $R^b$  is proportional to  $e^{qV/kT}$ . For a thin absorber (i.e., minority-carrier diffusion length  $L$  > absorber thickness  $W$ ) with negligible surface recombination at the back contact, the quasi-Fermi level separation is constantly  $V$  in the entire QNR. Therefore, the recombination coefficients can be expressed as

$$\begin{cases} R_0^i = S_h N_V \exp\left(\frac{-q\phi_{b0}}{kT}\right) \\ R_0^d = \frac{W_d}{\tau_e + \tau_h} n_i \\ R_0^b = \frac{W}{\tau_e} \frac{n_i^2}{N_A} \end{cases} \quad (2)$$

In Eq. (2),  $S_h$  is the surface recombination velocity for holes at the buffer/absorber interface,  $N_V$  is the effective density of state in the valence band of the absorber,  $\phi_{b0}$  is the hole potential barrier at the buffer/absorber interface at zero bias,  $W_d$  is the depletion width in the absorber,  $\tau_e$  is the electron lifetime in the absorber,  $\tau_h$  is the hole lifetime in the absorber,  $n_i$  is the intrinsic carrier density of the absorber,  $W$  is the absorber thickness, and  $N_A$  is the majority carrier (hole) density. For a thick absorber (i.e.,  $L \ll W$ ), the minority-carrier distribution decays exponentially (the decay length being  $L$ ) away from the SCR, and the spatial integration of  $R^b$  leads to replacement of  $W$  by  $L$  in the expression of  $R_0^b$  in Eq. (2). Eqs. (1) and (2) describe factors governing recombination rates in each region. At the interface,  $R^i$  is proportional to the surface recombination velocity and density of holes (majority carriers) there. In the SCR,  $R^d$  is proportional to the space-charge width, the inverse sum of lifetimes of both carriers, and the density of either carrier where they equal each other. In the QNR,  $R^b$  is proportional to a length characterizing the effective recombination volume (e.g.,  $W$  for a thin absorber and  $L$  for a thick absorber as described above), inverse lifetime of electrons, and density of electrons (minority carriers).

By equating the total recombination to generation at  $V=V_{OC}$ , i.e.,  $GW = R^i + R^d + R^b$ , one uses Eq. (1) to solve the quadratic

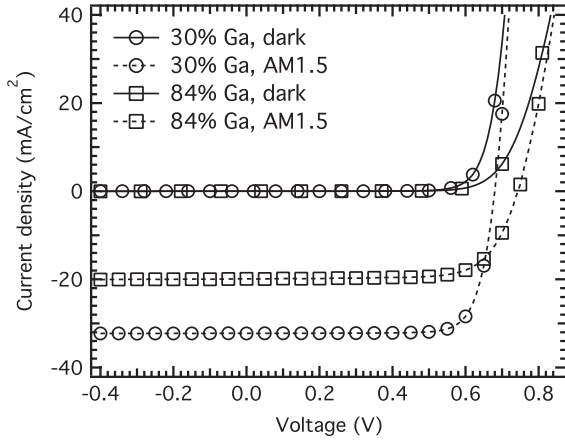


**Fig. 2.** Light (solid line) and dark (dashed line) current–voltage characteristics measured from the 30% (circles) and 84% (squares) Ga devices. The power conversion efficiency and  $V_{OC}$  are 17.4% and 682 mV for the 30% Ga device and 10.8% and 743 mV for the 84% Ga device, respectively.

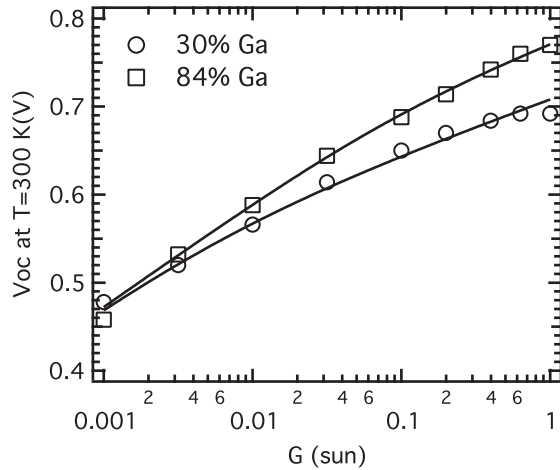


**Fig. 3.** The dependence of  $V_{OC}$  on light-intensity  $G$  for both the 30% and 84% Ga devices at 300 K. The experimental data taken from the CIGS device with 30% Ga (circles) are fitted (line) to Eq. (3) for extraction of  $R_0^i + R_0^b = 3.4 \times 10^5$  and  $R_0^d = 3.3 \times 10^{10} \text{ cm}^{-2} \text{ s}^{-1}$ . The experimental data taken from the CIGS device with 84% Ga (squares) are fitted (solid line) to Eq. (3) for extraction of  $R_0^i + R_0^b = 2.2 \times 10^4$  and  $R_0^d = 3.3 \times 10^{10} \text{ cm}^{-2} \text{ s}^{-1}$ .

equation for  $e^{qV/2kT}$  and then for  $V_{OC}$

$$V_{OC} = \frac{2kT}{q} \ln \left[ \frac{1}{2} \frac{R_0^d}{R_0^i + R_0^b} \left( \sqrt{4GW \frac{R_0^i + R_0^b}{(R_0^d)^2} + 1} - 1 \right) \right]. \quad (3)$$

$V_{OC}$  is uniquely determined by recombination coefficients, generation, and temperature, the latter two being experimentally controllable. It can be seen from Eq. (2) that the recombination coefficients depend sensitively on  $T$ , but not on  $G$ . Therefore, one can extract  $R_0^i + R_0^b$  and  $R_0^d$  by fitting Eq. (3) to experimental  $V_{OC}(G)$  data (e.g., Figs. 2 and 3) taken at a fixed temperature, usually 300 K. In the limit of  $4GW(R_0^i + R_0^b)(R_0^d)^{-2} \gg 1$ , the activation energy of recombination  $E_a$  (i.e., the intercept of  $V_{OC}(T)$  at  $T = 0$  K; see Fig. 4 for example) is the mean of absorber bandgap  $E_g$  and hole potential barrier  $q\phi_{b0}$  at the interface at zero bias (Fig. 1) weighted by  $R_0^i$  and  $R_0^b$ .

$$E_a = \frac{R_0^i q\phi_{b0} + R_0^b E_g}{R_0^i + R_0^b} \quad (4)$$

With knowledge of  $E_g$  and  $\phi_{b0}$  (extracted from capacitance–voltage measurement, see Figs. 1 and 5), the ratio  $R_0^i/R_0^b$  is calculated from

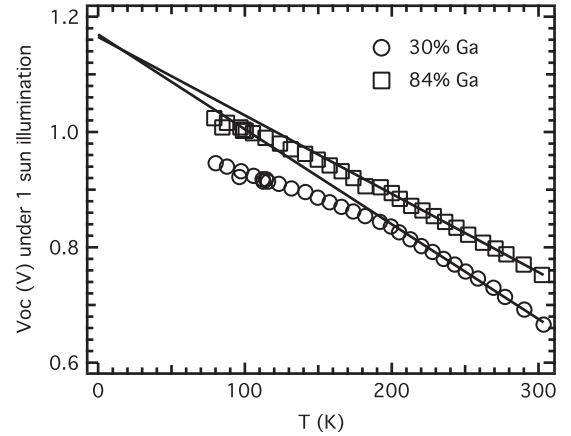


**Fig. 4.** The dependence of  $V_{OC}$  on temperature  $T$  under 1-sun illumination. The experimental data taken from the CIGS device with 30% Ga (circles) are fitted to a line for extraction of  $E_a = 1.17$  eV, which yields  $R_0^i/R_0^b = 0.1$  from Eq. (4). The experimental data taken from the CIGS device with 84% Ga (squares) are fitted to a line for extraction of  $E_a = 1.16$  eV, which yields  $R_0^i/R_0^b = 10$  from Eq. (4).

$E_a$ . Knowing both  $R_0^i + R_0^b$  and  $R_0^i/R_0^b$  allows one to solve the recombination coefficients at the interface  $R_0^i$  and in the QNR  $R_0^b$ . We then calculate the actual recombination rates in each region  $R^i$ ,  $R^b$ , and  $R^d$  at  $V = V_{OC}$  from Eq. (1). Finally, Eq. (2) enables the extraction of material and device properties such as electron lifetime  $\tau_e$ , surface recombination of holes  $S_h$ , hole lifetime  $\tau_h$ , and depletion width  $W_d$ . Note that all recombination rates and associated parameters should be regarded as “effective” values averaged out in the respective region. Only the lowest point of the bandgap is used because our devices contain intentional bandgap-grading.

#### 4. Results

The performance of the devices is shown by the dark and light current–voltage characteristics in Fig. 2. The power conversion efficiency  $\eta$  of the 30% Ga device is 17.4% with a  $V_{OC}$  of 0.682 V, a short-circuit current density of 32.3 mA/cm², and a fill factor of 79.2%. The power conversion efficiency  $\eta$  of the 84% Ga device is 10.8% with a  $V_{OC}$  of 0.743 V, a short-circuit current density of 19.8 mA/cm², and a fill factor of 72.9%. The best cell efficiencies for these two samples are 17.9% and 11.5%, respectively, representing the current state of the art in the respective ranges of Ga composition.

We plot the light-intensity-dependent  $V_{OC}(G)$  data measured at 300 K in Fig. 3 and the temperature-dependent  $V_{OC}(T)$  data measured under 1-sun illumination in Fig. 4. Note that the shunt resistance may suppress  $V_{OC}$  if  $G$  is too low. For both devices, this effect occurs below 0.001 sun. For the sample with 30% Ga CIGS absorber, we fit the experimental  $V_{OC}(G)$  data (circles in Fig. 3) to Eq. (3) to extract  $R_0^i + R_0^b = 3.4 \times 10^5 \text{ cm}^{-2} \text{ s}^{-1}$  and  $R_0^d = 3.3 \times 10^{10} \text{ cm}^{-2} \text{ s}^{-1}$ . At this point, we verify that  $4GW(R_0^i + R_0^b)(R_0^d)^{-2} = 400 \gg 1$ . This inequality allows us to use Eq. (4) to obtain  $R_0^i/R_0^b = 0.1$  from  $E_a = 1.17$  eV (extracted from  $V_{OC}(T)$  data in Fig. 4),  $E_g = 1.18$  eV, and  $\phi_{b0} = 1.00$  V. We extracted  $\phi_{b0}$  by summing the built-in voltage in the CIGS absorber;  $\phi_{bi,CIGS} = 0.78$  V, extracted by the Mott–Schottky method in Fig. 5(a); and  $\zeta_b/q = 0.22$  V, where  $\zeta_b$  is the bulk Fermi level in CIGS calculated from  $N_V = 1.8 \times 10^{19} \text{ cm}^{-3}$  taken from Ref. [20] and  $N_A = 0.5 \times 10^{16} \text{ cm}^{-3}$  measured by the capacitance–voltage method in Fig. 5(b). Combining  $R_0^i + R_0^d$  and  $R_0^i/R_0^b$  yields  $R_0^i = 3.1 \times 10^4 \text{ cm}^{-2} \text{ s}^{-1}$  and  $R_0^b = 3.1 \times 10^5 \text{ cm}^{-2} \text{ s}^{-1}$ . Then we use Eq. (1) to calculate the individual recombination rates at the  $V_{OC}$  point

$R^i = 1.4 \times 10^{16} \text{ cm}^{-2} \text{ s}^{-1}$ ,  $R^d = 2.2 \times 10^{16} \text{ cm}^{-2} \text{ s}^{-1}$ , and  $R^b = 1.4 \times 10^{17} \text{ cm}^{-2} \text{ s}^{-1}$ . Note that  $R^b$  is the largest of all three recombination rates, indicating that QNR recombination dominates  $V_{OC}$  for the 30% Ga device. From  $R_0^b$  and  $R_0^i$ , we use Eq. (2) to obtain the bulk minority-carrier lifetime  $\tau_e = 64 \text{ ns}$  and surface recombination velocity  $S_h = 2.6 \times 10^3 \text{ cm/s}$ , respectively.

For the sample with the 84% Ga CIGS absorber, we use the same procedure to extract the recombination coefficients  $R_0^i = 2.0 \times 10^4 \text{ cm}^{-2} \text{ s}^{-1}$ ,  $R_0^d = 3.3 \times 10^{10} \text{ cm}^{-2} \text{ s}^{-1}$ , and  $R_0^b = 2.0 \times 10^3 \text{ cm}^{-2} \text{ s}^{-1}$ . We extracted  $\phi_{b0} = 1.12 \text{ V}$  by summing the built-in voltage in the CIGS absorber;  $\phi_{bi,CIGS} = 0.90 \text{ V}$ , extracted by the Mott–Schottky method in Fig. 5(a); and  $\zeta_b/q = 0.22 \text{ V}$ , where  $\zeta_b$  is the bulk Fermi level in CIGS calculated from  $N_V = 1.8 \times 10^{19} \text{ cm}^{-3}$  taken from Ref. [20] and  $N_A = 0.5 \times 10^{16} \text{ cm}^{-3}$  measured by the capacitance–voltage method in Fig. 5(b). Note that the same  $N_V$  is

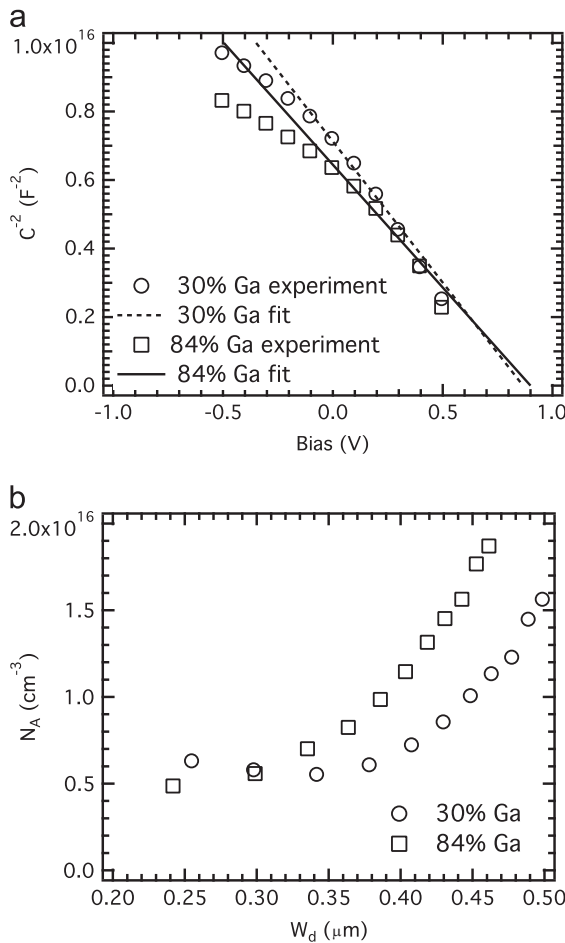


**FIG. 5.** (a) The Mott–Schottky plots for 30% Ga (circles) and 84% Ga (squares) measured at 10 kHz and 300 K are used to extract the built-in voltage, which is about  $\phi_{bi,CIGS}$  when the band bending in the buffer is neglected. Five data points from 0 to +0.4 V bias are used for the linear fitting to yield  $\phi_{bi,CIGS}$  of 0.78 V and 0.90 V for the 30% Ga and 84% Ga devices, respectively. (b) The depth profiles of carrier density calculated from the capacitance–voltage measurement at 10 kHz and 300 K are used to extract majority-carrier density  $N_A = 0.5 \times 10^{16} \text{ cm}^{-3}$  and the bulk Fermi level  $\zeta_b = 0.22 \text{ eV}$  in CIGS for both devices.  $N_A$  is taken from the lowest point of the curve to minimize the effect of deep levels.

**Table 1**

Summary of device performance and extracted recombination parameters.

Ga (%)	$V_{OC}$ (mV)	$\eta$ (%)	$R^i$ ( $\text{cm}^{-2} \text{ s}^{-1}$ )	$R^d$ ( $\text{cm}^{-2} \text{ s}^{-1}$ )	$R^b$ ( $\text{cm}^{-2} \text{ s}^{-1}$ )	$R_0^i$ ( $\text{cm}^{-2} \text{ s}^{-1}$ )	$R_0^d$ ( $\text{cm}^{-2} \text{ s}^{-1}$ )	$R_0^b$ ( $\text{cm}^{-2} \text{ s}^{-1}$ )	$\tau_e$ (ns)	$S_h$ (cm/s)	$E_a$ (eV)	$E_g$ (eV)
30	682	17.4	$1.4 \times 10^{16}$	$2.2 \times 10^{16}$	$1.4 \times 10^{17}$	$6.4 \times 10^4$	$3.3 \times 10^{10}$	$3.4 \times 10^5$	64	$2.6 \times 10^3$	1.17	1.18
84	743	10.8	$9.1 \times 10^{16}$	$7.0 \times 10^{16}$	$9.1 \times 10^{15}$	$2.0 \times 10^4$	$3.3 \times 10^{10}$	$2.0 \times 10^3$	< 0.05	$7.9 \times 10^3$	1.16	1.50

used for both samples because of a lack of available data, but it could change with Ga composition if the effective mass of holes is changed. The recombination rates are  $R^i = 9.1 \times 10^{16} \text{ cm}^{-2} \text{ s}^{-1}$ ,  $R^d = 7.0 \times 10^{16} \text{ cm}^{-2} \text{ s}^{-1}$ , and  $R^b = 9.1 \times 10^{15} \text{ cm}^{-2} \text{ s}^{-1}$ . Note that  $R^i$  is the largest of all three recombination rates, indicating that interface recombination dominates  $V_{OC}$  for the 84% Ga absorber. From  $R_0^d$  and  $R_0^i$ , we obtain  $\tau_e = 0.05 \text{ ns}$  and  $S_h = 7.9 \times 10^3 \text{ cm/s}$  in this device. The recombination parameters extracted from both the low-Ga and high-Ga devices are summarized in Table 1.

To verify accuracy of some of the aspects of the  $V_{OC}(T)$  analysis described above, we used TRPL measurement to independently measure minority-carrier lifetime. TRPL measurements were carried out on CIGS absorbers immediately after deposition to avoid possible degradation effects [21]. Fig. 6a shows that TRPL decay for CIGS absorber with 30% Ga is single-exponential and has  $\tau_e = 317 \text{ ns}$  lifetime. In contrast, TRPL decay for CIGS film with 84% Ga has a very short lifetime. Deconvolution of the

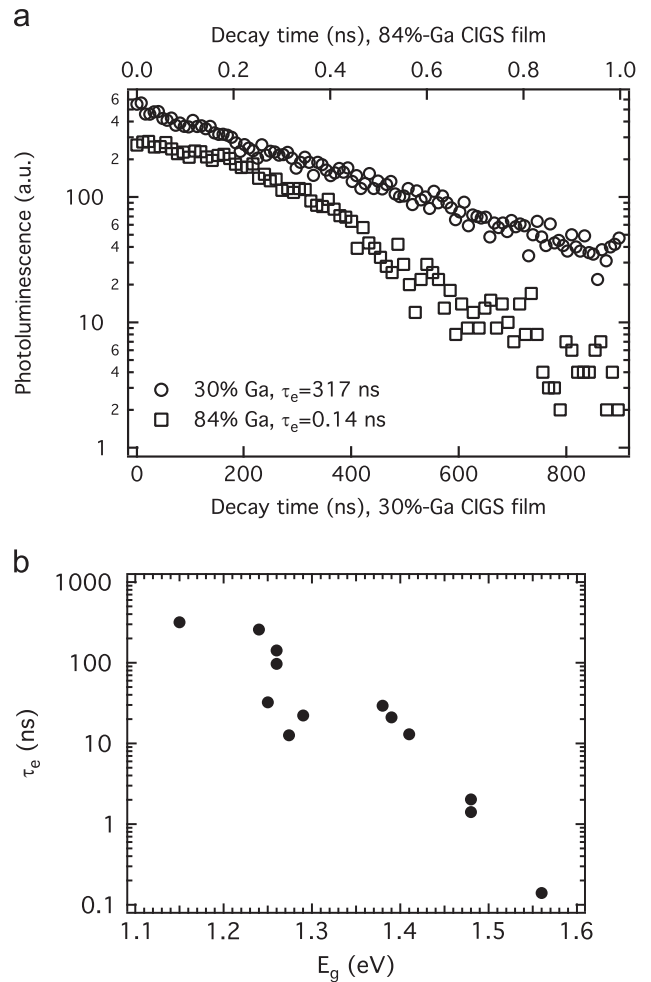


**FIG. 6.** (a) The semi-logarithmic display of time-resolved photoluminescence (TRPL) decays for CIGS films with 30% Ga (circles) and 84% Ga (squares). Linear fittings yield minority-carrier lifetime of 317 and 0.14 ns, respectively. (b) The TRPL-measured minority-carrier lifetimes are displayed against the bandgap of CIGS films varied due to Ga composition.



instrumental response [22] was used to determine  $\tau_e = 0.14$  ns. Fig. 6b shows the TRPL lifetime dependence on Ga composition for additional CIGS films. Lifetime decreases by more than three orders of magnitude when the Ga composition increases from 30% to 84%. Within experimental error and material fluctuation, the lifetime values extracted above by  $V_{OC}(G,T)$  analysis agree well with TRPL results.

Assuming electron mobility of  $100 \text{ cm}^2 \text{ V}^{-1} \text{ s}^{-1}$ , we further estimate the minority-carrier diffusion length  $L$  to be 4.5 and  $0.1 \text{ }\mu\text{m}$  for the 30% and 84% Ga devices, respectively, which is consistent with the quantum efficiency (data not shown) and cross-sectional scanning electron-beam-induced current experiment (Figs. 5 and 8 in Ref. [4] for low- and high-Ga samples, respectively, similar to those used in this study). For the device with 30% Ga, the thin-absorber approximation holds and Eq. (2) is valid for extraction of  $\tau_e$ . However, for the device with 84% Ga,  $L \ll W$ , which indicates that the thick-absorber approximation should be used. Therefore,  $W$  should be replaced with  $L$  in the expression of  $R_0^b$  in Eq. (2), which leads to  $\tau_e = 0.2$  ps. However, this value is too close to those of other physical processes such as electron thermalization and drift in the pn junction. Some assumptions used in the  $V_{OC}(G,T)$  analysis do not accurately reflect the carrier recombination dynamics on such a short time scale. Therefore, we can only use 0.05 ns as the upper limit of electron lifetime for the device with 84% Ga.

## 5. Discussion

We now inspect more closely the recombination coefficients and rates in the context of varying bandgap energy. To do so, we rearrange Eqs. (1) and (2) to express all the recombination rates in similar forms

$$\begin{cases} R^i = R_0^i e^{qV/kT} = S_h N_V \exp\left(\frac{\zeta_i - E_g}{kT}\right) \exp\left(\frac{qV}{kT}\right) \\ R^d = R_0^d e^{qV/2kT} = \frac{W_d}{\tau_e + \tau_h} \sqrt{N_C N_V} \exp\left(\frac{-E_g}{2kT}\right) \exp\left(\frac{qV}{2kT}\right) \\ R^b = R_0^b e^{qV/kT} = \frac{W}{\tau_e} \frac{N_C N_V}{N_A} \exp\left(\frac{-E_g}{kT}\right) \exp\left(\frac{qV}{kT}\right) \end{cases} \quad (5)$$

In Eq. (5),  $N_C$  is the effective density of states in the conduction band of the absorber,  $\zeta_i$  is the separation of Fermi energy  $E_F$  from the conduction band  $E_C$  at the buffer/absorber interface, and  $\zeta_b$  is the separation of Fermi energy  $E_F$  from the valence band  $E_V$  in the QNR of the absorber. Each recombination rate is thus the product of four terms. From left to right, these four terms are: (i) a recombination velocity; here, we refer to  $W_d/(\tau_e + \tau_h)$  as the SCR recombination velocity and  $W/\tau_e$  as the QNR recombination velocity; (ii) an intrinsic carrier density, which is a fundamental property of the absorber; (iii) the dependence of the recombination-dominating carrier density on material (bandgap and doping) and junction (band-bending) properties, which will be discussed more extensively in the next sections; and (iv) the exponential bias dependence. Note that although  $N_A$  is constant over temperature [11,16] in most cases, it could vary with temperature according to the Boltzmann approximation of  $N_V \exp(-\zeta_b/kT)$ . The former scenario is often true near room temperature and yields  $E_a = E_g$ . The latter scenario may be true at lower temperatures (or if the dopants levels are relatively deep) and yields  $E_a = E_g - \zeta_b$ —i.e., term (ii) changes to  $(\zeta_b - E_g)/kT$ .

The fourth term in Eq. (5) indicates that the recombination rates increase exponentially with bias, but with different exponents:  $qV/2kT$  for  $R^d$  as opposed to  $qV/kT$  for  $R^i$  and  $R^b$ . Although the SCR recombination coefficient  $R_0^d$  is much larger (Table 1) than that of either the interface  $R_0^i$  or the QNR  $R_0^b$ , the SCR recombination rate  $R^d$  only dominates at low to moderate biases. Because the function  $e^{qV/kT}$  is much faster than  $e^{qV/2kT}$ , the SCR recombination

rate  $R^d$  is eventually overtaken by those at the interface  $R^i$  and in QNR  $R^b$  at high biases. Especially in the state-of-the-art CIGS devices used in this study (Table 1), the recombination rate in the SCR  $R^d$  at  $V_{OC}$  is less than the sum of those at the interface and QNR  $R^i + R^b$ . Therefore,  $V_{OC}$  of these devices are limited by either interface recombination or QNR recombination.

The third term in Eq. (5) contains an exponential dependence on the bandgap energy:  $\exp(-E_g/kT)$ . This suggests that, all else being equal, the recombination coefficients as well as rates in all three regions decrease exponentially with increasing bandgap energy of the absorber. Considering that the generation rate  $G$  due to the sun spectrum only decreases slightly with  $E_g$ ,  $V_{OC}$  increases linearly to the first order with  $E_g$  because  $V_{OC} = \ln(GW/R_0^{\text{dominant}})nkT/q$ , where  $R_0^{\text{dominant}}$  is the coefficient of the dominant recombination mechanism and  $n=1$  or  $2$  depending on the dominant recombination mechanism. This is the rationale for pursuing higher-bandgap absorbers. Up to a point,  $V_{OC}$  indeed increases linearly with  $E_g$  in experiment ([4,13–15]). Beyond that, other factors overrule the benefit of recombination reduction by increasing  $E_g$ . We discuss some of these factors below.

Next, we focus on a detailed comparison of the interface and QNR recombination, which also expands the discussion on the third term in Eq. (5). We obtain an expression for the ratio of  $R^i/R^b$  from Eq. (5)

$$\frac{R^i}{R^b} = \frac{N_A}{N_C} \frac{S_h}{W/\tau_e} \exp\left(\frac{\zeta_i}{kT}\right). \quad (6)$$

The voltage-dependence term in Eq. (5) disappears because it is the same for  $R^i$  and  $R^b$ . The right-hand side of Eq. (6) consists of three terms. The first term  $N_A/N_C$  is intrinsic to the material, and it can be improved through engineering of doping ( $N_A$ ) or effective mass ( $N_C$ ). The second term  $S_h/W\tau_e^{-1}$  is the ratio between the recombination velocity at the interface and that in the QNR (i.e.,  $W\tau_e^{-1}$ ). This term evaluates the material quality of the interface relative to that of the QNR in terms of its recombination effectiveness. For a specific absorber with minority-carrier lifetime  $\tau_e$ , it is desirable to have  $S_h < W\tau_e^{-1}$  in order for the interface recombination quality to surpass that of the QNR. Obviously, a large  $W$  helps. Alternatively,  $S_h$  needs to be sufficiently small. An example is for  $\tau_e = 100$  ns and  $W = 2 \text{ }\mu\text{m}$ , where  $S_h$  needs to be  $< 2 \times 10^3 \text{ cm/s}$  for the interface material quality to be superior to that of the QNR.

Unlike the first two terms, the third term  $\exp(\zeta_i/kT)$  in Eq. (6) is intrinsic not to material, but rather, to device architecture because it is an assessment of the inversion strength ( $\zeta_i$ ) at the interface. The stronger the inversion, the smaller is the value of  $\zeta_i$ , and hence, the less significant is interface recombination compared to bulk recombination. Therefore, a strong inversion helps to tolerate an interface with poor recombination quality characterized by large  $S_h$ . This is the rationale behind the pursuit of alternative buffers with proper band offset. A “spike” type offset between the conduction bands of the absorber and the buffer (as shown in Fig. 1) provides the necessary potential confinement to minority carriers, thus favoring inversion. This is an especially important subject for devices of higher-bandgap absorbers due to shifts of the conduction and valence bands.

Compared to the low-Ga sample, it is surprising that  $R^i/R^b$  is  $\sim 100$  times higher in the high-Ga sample considering  $\tau_e$  is at least  $\sim 1000$  times worse. One obvious factor is  $R_0^b$ , which is proportional to  $W$  ( $2 \text{ }\mu\text{m}$ ) for the low-Ga sample but to  $L$  ( $10 \text{ nm}$ ) for the high-Ga sample according to Eq. (2). A more important key lies in  $\zeta_i$ , which is  $0.1$  and  $0.38 \text{ eV}$  in the low-Ga and high-Ga samples, respectively. Since  $\zeta_b$  is  $\sim 0.22 \text{ eV}$  for both samples, a strong inversion is achieved in the low-Ga sample but not in the high-Ga sample. According to Eq. (6),  $R^i/R^b$  is dominated by  $\exp(-\zeta_i/kT)$ . For a  $\zeta_i$  difference of  $0.28 \text{ eV}$ ,  $\exp(-0.28 \text{ eV}/kT) = 5.2 \times 10^4$ , causing

$R^i/R^b$  to be  $\sim 100$  times higher in the high-Ga sample despite lower  $\tau_e$ . Therefore, the reason for  $V_{OC}$  to be limited by interface recombination in the high-bandgap devices is essentially a weakness or even absence of inversion due to insufficient band bending in the absorber. Because  $R^i/R^b$  increases with decreasing temperature according to Eq. (6), the interface recombination becomes more dominant at lower temperatures for the high-Ga sample (recall that  $R^i/R^b = 10$  at room temperature). According to Eq. (4),  $E_a = 1.16$  eV is already very close to  $q\phi_{b0} = 1.12$  eV at room temperature. At lower temperatures,  $E_a$  becomes even closer to  $q\phi_{b0}$ , but the numerical change is small because of the large  $R^i/R^b$  value, resulting in a  $V_{OC}(T)$  curve with a constant slope over the entire temperature range in Fig. 4. For the low-Ga sample, the smaller  $E_a$  below 200 K could indicate either:  $R^i/R^b$  growing to  $> 1$  below 200 K, hence, becoming interface recombination dominant; or, majority-carrier density  $N_A$  ceasing to be temperature independent below 200 K, hence,  $E_a$  changing from  $E_g$  to  $E_g - \zeta_b$ .

How then does one increase inversion at the interface? Fig. 1 shows that  $\zeta_i = E_g - q\phi_{bi,CIGS} - \zeta_b$ , where  $\phi_{bi,CIGS}$  is the band bending in the CIGS absorber. Suppressing interface recombination by strong inversion (low  $\zeta_i$ ) is thus inherently more challenging as  $E_g$  increases. Increasing  $\zeta_b$  by reducing doping in CIGS directly reduces  $R^i/R^b$  by reducing  $\zeta_i$ , although this effect may be compromised by an accompanying reduction in  $\phi_{bi,CIGS}$ . For the purpose of reducing  $\zeta_i$ , by far the most rewarding strategy is to pursue higher  $\phi_{bi,CIGS}$ —a figure of merit more effectively engineered via optimization of device architecture than material quality.

Based on the above results and discussion, we compare the high-Ga state-of-the-art absorbers with their low-Ga counterparts to summarize the major mechanisms limiting the present performance and mitigation strategies: (i) A higher  $E_g$  reduces recombination rates due to their exponential dependence  $\exp(-E_g/kT)$  in Eq. (5). This is the main driver for potential higher performance in high-Ga absorbers and is experimentally observed in the linear increase of  $V_{OC}$  with  $E_g$  up to a point. (ii) As shown by both the  $V_{OC}(T,G)$  analysis and TRPL in Fig. 6(b), the bulk minority-carrier lifetime  $\tau_e$  is much smaller in high-Ga absorbers, which suggests that these materials are more defective and in need of improvement (e.g., by tuning growth temperature [4]). (iii) The surface recombination velocity  $S_h$  being only moderately higher indicates that the recombination quality of the CdS/CIGS interface is not significantly deteriorated by a higher  $E_g$ . (Note that the recombination rate depends on two factors: the recombination quality—that is, effectiveness of recombination characterized by lifetime and surface recombination velocity—and carrier density.) This suggests that a satisfactory passivation effect may be achieved by chemical-bath-deposited CdS on high-Ga CIGS absorbers. (iv) Because the conduction band-edge  $E_C$  moves up with Ga composition [23], the buffer/absorber band offset becomes less favorable for inversion [this is the carrier density factor mentioned in (iii)], thus increasing the interface recombination rate  $R^i$ . This can be mitigated by alternative buffers with lower electron affinity to achieve proper conduction band offset. (v) The hole density  $N_A$  is essentially unchanged, which means the same Fermi-level positioning relative to  $E_V$  (i.e.,  $\zeta_b$ )—a fortunate situation requiring no further improvement in doping for the moment. (vi) Neither a higher  $E_g$  nor a higher  $E_C$  in the absorber increases the built-in voltage (i.e., total band-bending in the heterojunction). Because the built-in voltage is determined by the difference of  $E_F$  in the bulk of the TCO and CIGS absorber (see Fig. 1), nothing short of raising  $E_F$  on the n-type side (TCO most likely dominates the buffer) or lowering  $E_F$  on the p-type side can be effective at increasing it directly. Since both  $\zeta_b$  and  $E_V$  on the p-type side is relatively unchanged by Ga composition (although alloying with sulfur may be more effective in lowering  $E_V$  and  $E_F$  while achieving higher  $E_g$ ), an alternative TCO with low work function is more promising for

raising  $E_F$  on the n-side and directly enhancing the total band-bending of the heterojunction. This, in turn, increases  $\phi_{bi,CIGS}$ , which decreases the interface-vs-bulk recombination ratio in Eq. (6). (vii) Unlike the case of the low-Ga absorber [24], it is unclear whether a homojunction can be formed entirely in the high-Ga CIGS absorber. In optimized n-type CIGS,  $E_F$  is close to  $E_C$  and will move up with  $E_C$  as Ga composition increases. Therefore, a homojunction in the high-Ga CIGS may enable higher  $\phi_{bi,CIGS}$  than the buffer/CIGS heterojunction, where  $\phi_{bi,CIGS}$  is limited by the relative immovability of  $E_F$  on the n-side with increasing Ga composition. In high-Ga absorbers, a CIGS homojunction is thus superior to a heterojunction architecture for achieving higher  $\phi_{bi,CIGS}$ , lower interface recombination, and higher  $V_{OC}$ .

## 6. Conclusions

We demonstrate that the recently developed formulation of  $V_{OC}(T,G)$  is effective in separating and quantifying individual recombination rates at the buffer/absorber interface, in the SCR, and in the QNR, as well as the bulk minority-carrier lifetime and surface recombination velocity at the buffer/absorber interface of thin-film CIGS solar cells. In the low-bandgap absorbers, recombination in the quasi-neutral region dominates. In the high-bandgap absorbers, interface recombination dominates because of a lack of strong inversion at the interface caused by insufficient band bending in the absorber. The  $V_{OC}$  deficit in high-bandgap devices originates from an inadequacy of band bending in the absorber and a weakness or absence of inversion at the buffer/absorber interface. Reducing interface recombination is inherently more challenging in high-bandgap devices and should take priority. In particular, it is imperative to engineer the absorber/buffer/TCO junction to achieve higher band-bending in the absorber and stronger inversion at the interface. The CIGS homojunction or alternative n-TCOs with low work function are two promising mitigating strategies for the  $V_{OC}$  deficit problem at high-Ga levels.

## Acknowledgments

The authors thank Dr. Ingrid Repins at the National Renewable Energy Laboratory for her critical review that resulted in substantial improvements to this manuscript. The authors also thank the reviewers for their comments that improved this manuscript. The authors benefited from discussion with Dr. Rafael Jaramillo and Riley Brandt at the Massachusetts Institute of Technology, and Wes Miller at the University of Oregon. This research is supported by the U.S. Department of Energy under Contract No. DE-AC36-08GO28308.

## References

- [1] H.-W. Schock, R. Noufi, CIGS-based solar cells for the next millennium, *Prog. Photovolt.: Res. Appl.* 8 (2000) 151–160.
- [2] A. Chirila, P. Reinhard, F. Pianezzi, P. Bloesch, A.R. Uhl, C. Fella, L. Kranz, D. Keller, C. Gretener, H. Hagendorfer, D. Jaeger, R. Erni, S. Nishiwaki, S. Buecheler, A.N. Tiwari, Potassium-induced surface modification of Cu(In,Ga)Se<sub>2</sub> thin films for high-efficiency solar cells, *Nat. Mater.* 12 (2013) 1107–1111.
- [3] P. Jackson, D. Hariskos, E. Lotter, S. Paetel, R. Wuerz, R. Menner, W. Wischmann, M. Powalla, New world record efficiency for Cu(In,Ga)Se<sub>2</sub> thin-film solar cells beyond 20%, *Prog. Photovolt.: Res. Appl.* 19 (2011) 894–897.
- [4] M.A. Contreras, L.M. Mansfield, B. Egaas, J. Li, M. Romero, R. Noufi, E. Rudiger-Voigt, W. Mannstadt, Wide bandgap Cu(In,Ga)Se<sub>2</sub> solar cells with improved energy conversion efficiency, *Prog. Photovolt.: Res. Appl.* 20 (2012) 843–850.
- [5] M. Turcu, I.M. Kotschau, U. Rau, Composition dependence of defect energies and band alignments in the Cu(In<sub>1-x</sub>Ga<sub>x</sub>)(Se<sub>1-y</sub>S<sub>y</sub>)<sub>2</sub> alloy system, *J. Appl. Phys.* 91 (2002) 1391–1399.
- [6] S. Siebentritt, U. Rau, *Wide-Gap Chalcopyrites*, Springer, Berlin, Germany, 2005.

- [7] J.R. Sites, Separation of voltage loss mechanisms in polycrystalline solar cells, in: Proceedings of the 20th IEEE Photovoltaic Specialist Conference, Las Vegas, USA, 1988, pp. 1604–1607.
- [8] J.T. Heath, J.D. Cohen, W.N. Shafarman, D.X. Liao, A.A. Rockett, Effect of Ga content on defect states in  $\text{CuIn}_{1-x}\text{Ga}_x\text{Se}_2$  photovoltaic devices, *Appl. Phys. Lett.* 80 (2002) 4540–4542.
- [9] T. Minemoto, Y. Hashimoto, T. Satoh, T. Negami, H. Takakura, Y. Hamakawa, Cu(In,Ga)Se<sub>2</sub> solar cells with controlled conduction band offset of window/Cu(In,Ga)Se<sub>2</sub> layers, *J. Appl. Phys.* 89 (2001) 8327–8330.
- [10] S. Siebentritt, Alternative buffers for chalcopyrite solar cells, *Sol. Energy* 77 (2004) 767–775.
- [11] U. Rau, H.W. Schock, Electronic properties of Cu(In,Ga)Se<sub>2</sub> heterojunction solar cells – recent achievements, current understanding, and future challenges, *Appl. Phys. A Mater. Sci. Process.* 69 (1999) 131–147.
- [12] S.S. Hegedus, W.N. Sharfarman, Thin-film solar cells: device measurements and analysis, *Prog. Photovolt.: Res. Appl.* 12 (2004) 155–176.
- [13] R. Herberholz, V. Nadenau, R. Ruhle, C. Koble, H.W. Schock, B. Dimmler, Prospects of wide-gap chalcopyrites for thin-film photovoltaic modules, *Sol. Energy Mater. Sol. Cells* 49 (1997) 227–237.
- [14] I. Hengel, A. Neisser, R. Klenk, M.Ch. Lux-Steiner, Current transport in  $\text{CuInS}_2$ :Ga/CdS/ZnO solar cells, *Thin Solid Films* 361–362 (2000) 458–462.
- [15] M. Turcu, U. Rau, Fermi level pinning at CdS/Cu(In,Ga)(Se,S)<sub>2</sub> interfaces: effect of chalcopyrite alloy composition, *J. Phys. Chem. Solids* 64 (2003) 1591–1595.
- [16] S. Grover, J.V. Li, D.L. Young, P. Stradins, H.M. Branz, Reformulation of solar cell physics to facilitate experimental separation of recombination pathways, *Appl. Phys. Lett.* 103 (2013) (093502-1–093502-5).
- [17] D. Kuciauskas, J.N. Duenow, A. Kanevce, J.V. Li, M.R. Young, D.H. Levi, Optical-fiber-based time resolved photoluminescence spectrometer for thin film absorber characterization and analysis of TRPL data for CdS/CdTe interface, in: Proceedings of the 38th IEEE Photovoltaic Specialist Conference, Austin, USA, 2012, pp. 1721–1726.
- [18] W. Shockley, W.T. Read, Statistics of the recombination of holes and electrons, *Phys. Rev.* 87 (1952) 835–842.
- [19] T. Walter, R. Herberholz, H.W. Schock, Distribution of defects in polycrystalline chalcopyrite thin films, *Solid State Phenom.* 51–52 (1996) 309–316.
- [20] M. Gloekler, A.L. Fahrenbruch, J.R. Sites, Numerical modeling of CIGS and CdTe solar cells: setting the baseline, in: Proceedings of the Third World Conference on Photovoltaic Energy Conversion, Osaka, Japan, 2003, pp. 491–494.
- [21] W.K. Metzger, I.L. Repins, M.A. Contreras, Long lifetimes in high-efficiency Cu(In,Ga)Se<sub>2</sub> solar cells, *Appl. Phys. Lett.* 93 (2008) (022110-1–022110-3).
- [22] D. Kuciauskas, J.V. Li, M.A. Contreras, J. Pankow, P. Dippo, M. Young, L.M. Mansfield, R. Noufi, D. Levi, Charge carrier dynamics and recombination in graded band gap  $\text{CuIn}_{1-x}\text{Ga}_x\text{Se}_2$  polycrystalline thin-film photovoltaic solar cell absorbers, *J. Appl. Phys.* 114 (2013) (154505-1–154505-6).
- [23] T. Schulmeyer, R. Kniese, R. Hunger, W. Jaegermann, M. Powalla, A. Klein, Influence of Cu(In,Ga)Se<sub>2</sub> band gap on the valence band offset with CdS, *Thin Solid Films* 451–452 (2004) 420–423.
- [24] K. Ramanathan, R. Noufi, J. Granata, J. Webb, J. Keane, Prospects for in situ junction formation in  $\text{CuInSe}_2$  based solar cells, *Sol. Energy Mater. Sol. Cells* 55 (1998) 15–22.